Materials Science & Engineering A

Microstructure and nanomechanical behavior of an additively manufactured (CrCoNiFe)94Ti2Al4 high-entropy alloy

--Manuscript Draft--

Manuscript Number:	MSEA-D-21-02748R1
Article Type:	Research Paper
Keywords:	High-entropy alloys; Additive manufacturing; nanoindentation; crystallographic orientation; Nanoscale creep behavior
Corresponding Author:	Jianying He, Ph.D. Norwegian University of Science and Technology Trondheim, NORWAY
First Author:	Siqi Liu
Order of Authors:	Siqi Liu
	Di Wan
	Shuai Guan
	Yuequn Fu
	Xiaobo Ren
	Zhiliang Zhang
	Jianying He, Ph.D.
Abstract:	Recent substantial studies indicate that high-entropy alloys (HEAs) possess superior mechanical performance, including exceptional strength, high creep resistance, etc. However, additive manufacturing (AM), a burgeoning manufacturing method, may induce extraordinary impacts on the resulting mechanical properties. For the additively manufactured (AM-ed) HEAs, the nanoscale mechanical performance and deformation mechanisms in accordance with the microstructural properties remain unclear. In this work, the microstructure and nanomechanical properties of an AM-ed (CrCoNiFe)94Ti2Al4 HEA were investigated. The local mechanical properties including hardness, elastic modulus, and nanoscale creep deformation, were explored by nanoindentation-based measurement. Simultaneously, the crystallographic orientation dependence on the mechanical behavior of AM-ed HEA was carried out by combining with electron backscattered diffraction (EBSD). It is found that the {101}-grain has the highest hardness and elastic modulus, whereas the creep resistance of {111}-grain is the greatest, with the indicators of the creep mechanism showing lattice diffusion is the dominant mechanism. Two different states of HEA, as-printed and heat-treated, were utilized to explore the effect of heat treatment. Heat treatment in the current study can increase the hardness and elastic modulus but decrease the creep resistance slightly. This work elucidates the underlying mechanisms of grain orientation dependence on nanomechanical properties and the effects of heat treatment. Moreover, it also sheds light on the particular creep behavior at the nanoscale and creep mechanism of the AM-ed (CrCoNiFe)94Ti2 Al4 HEA.

Microstructure and nanomechanical behavior of an additively manufactured $(CrCoNiFe)_{94}Ti_2Al_4$ high-entropy alloy

Siqi Liu [a], Di Wan [b,*], Shuai Guan [c], Yuequn Fu [a], Xiaobo Ren [d], Zhiliang Zhang [a], Jianying He [a,*]

[a] NTNU Nanomechanical Lab, Department of Structural Engineering, Norwegian University of Science and Technology (NTNU), Trondheim 7491, Norway

[b] Department of Mechanical and Industrial Engineering, Norwegian University of Science and Technology (NTNU), Trondheim 7491, Norway

[c] Advanced Manufacturing Technology Research Center, Department of Industrial and Systems Engineering, The Hong Kong Polytechnic University, Hung Hom, Kowloon, Hong Kong

[d] Materials and Nanotechnology, SINTEF Industry, NO- 7465 Trondheim, Norway

[*]Corresponding author.
E-mail addresses: di.wan@ntnu.no (D. Wan), and jianying.he@ntnu.no (J. He).

Abstract

Recent substantial studies indicate that high-entropy alloys (HEAs) possess superior mechanical performance, including exceptional strength, high creep resistance, etc. However, additive manufacturing (AM), a burgeoning manufacturing method, may induce extraordinary impacts on the resulting mechanical properties. For the additively manufactured (AM-ed) HEAs, the nanoscale mechanical performance and deformation mechanisms in accordance with the microstructural properties remain unclear. In this work, the microstructure and nanomechanical properties of an AM-ed $(CrCoNiFe)_{94}Ti_2Al_4$ HEA were investigated. The local mechanical properties including hardness, elastic modulus, and nanoscale creep deformation, were explored by nanoindentation-based measurement. Simultaneously, the crystallographic orientation dependence on the mechanical behavior of AM-ed HEA was carried out by combining with electron backscattered diffraction (EBSD). It is found that the {101}-grain has the highest hardness and elastic modulus, whereas the creep resistance of {111}-grain is the greatest, with the indicators of the creep mechanism showing lattice diffusion is the dominant mechanism. Two different states of HEA, as-printed and heat-treated, were utilized to explore the effect of heat treatment. Heat treatment in the current study can increase the hardness and elastic modulus but decrease the creep resistance slightly. This work elucidates the

underlying mechanisms of grain orientation dependence on nanomechanical properties and the effects of heat treatment. Moreover, it also sheds light on the particular creep behavior at the nanoscale and creep mechanism of the AM-ed $(CrCoNiFe)_{94}Ti_2Al_4$ HEA.

Keywords: High-entropy alloys, Additive manufacturing, Nanoindentation, Crystallographic orientation, Nanoscale creep behavior

1. Introduction

Since thousands of years ago, humans have been tuning metals' properties by adding a small number of alloying elements to a primary element, which is the conventional alloy design philosophy. The concept of high-entropy alloys (HEAs) was first proposed in 2004 [1]. Unlike conventional alloys, HEAs contain at least four principal elements in an equal or near-equal atomic ratio, and thus there is no distinction between solute and solvent atoms in HEAs [2,3]. Such a compositional characteristic often leads to increased configurational entropy and hence the formation of multicomponent solid solutions (i.e., fcc, bcc, or hcp) [4,5]. In the past decades, HEAs have garnered unparalleled attention due to their superior mechanical properties and performance compared to conventional alloys, including hardness, yield strength, creep resistance, and wear resistance, etc. [6]. Except for the high configurational entropy, sluggish atomic diffusion and large lattice distortion, which are the main inherent properties of HEAs, are responsible for their extraordinary mechanical properties. An fcc-type $(CrCoNiFe)_{94}Ti_2Al_4$ HEA was recently reported to have a good strength-ductility synergy, with a tensile strength reaching ~1.3 GPa and an elongation reaching 17%, demonstrating potential applications for the advanced structural materials [7,8].

Additive manufacturing (AM), also termed as 3D printing, is an emerging and disruptive technology that changes the way of designing and manufacturing products [9]. AM offers numerous advantages in comparison with the traditional methods such as rapid fabrication and outstanding shape-design freedom, and therefore it has a wide range of application prospects in many fields [10,11]. AM builds

up components directly from a 3D model layer-by-layer, AM-ed alloys thereby experience a complex thermal history involving repeated melting and rapid solidification as well as subsequent heating-cooling cycles after solidification [11,12]. Furthermore, the rapid cooling rate during the AM process can result in a remarkable solute-trapping effect which in turn minimizes the compositional segregation [13]. Therefore, in this study, this attractive $(CrCoNiFe)_{94}Ti_2Al_4$ HEA was fabricated via AM, more specifically laser engineered net shaping (LENS^{TM}), and its mechanical performance and corresponding deformation mechanisms were investigated at the nanoscale. It is worth noting that the LENS^{TM} process is a typical laser powder-blown AM technique that has been used to manufacture HEAs [14,15].

On account of the aforementioned unique nature of the AM method, the microstructures and mechanical properties of AM-ed HEA consequently appear to be distinct from those obtained by traditional manufacturing techniques. Research efforts on this $(CrCoNiFe)_{94}Ti_2Al_4$ HEA have focused on its macroscopic mechanical properties behavior and oxidation resistance [7,16]. Nevertheless, there are still no fundamental understandings of the mechanical behavior and the underlying deformation mechanisms of AM-ed $(CrCoNiFe)_{94}Ti_2Al_4$ HEA at the nanoscale, which require a deeper exploration and understanding.

As for the study on the nanomechanical behavior of this AM-ed HEA, nanoindentation is a powerful technique that can characterize the microscale heterogeneity that exists in the AM-ed samples with high sensitivity. Furthermore, nanoindentation tests on one single grain can be regarded as testing of a single crystal, which means the mechanical behavior of a single crystal could be extracted from a polycrystalline material by nanoindentation. Therefore, combining electron backscattered diffraction (EBSD) and nanoindentation can offer the potential to evaluate the local elastic-plastic properties at nanoscale and correlate the mechanical response with the local microstructure and crystallography,

thus providing new understanding and insights into the deformation behavior of AM-ed alloys and some basic deformation mechanisms for further study at larger scales.

Besides the measurement of hardness and elastic modulus, the nanoscale creep deformation can be quantitatively characterized by nanoindentation. HEAs have been reported to possess good creep resistance because of sluggish atomic diffusion and large lattice distortion [17,18]. However, AM usually causes high dislocation density and smaller grain sizes [19], and thus the creep property of AM-ed HEAs can conceivably be distinct from that of traditional HEAs. To our best knowledge, little work has been done so far on the creep mechanisms of AM-ed HEAs. Contrasting to traditional creep tests where creep occurs mainly at elevated temperatures, the nanoindentation creep test can be performed at ambient temperature, and it is less time-consuming than conventional macro-scale tests. In general, nanoindentation creep tests have two important inherent characteristics which are the origins contributing to the disparity between the nanoindentation creep and traditional uniaxial creep tests. On one hand, the stress distribution under nanoindentation creep could be much more complicated, and the maximum shear stress under the indenter tip exceeds the yield stress of the specimen in the process of nanoindentation creep testing, which is the reason for the creep occurrence at room temperature [20]. On the other hand, the stress state of the nanoindentation creep technique is tri-axially non-homogeneous, and the deformation volume underneath the indenter tip grows steadily, which is different from the conventional uniaxial creep tests [21].

Based on this background, the LENS^{TM}-processed $(CrCoNiFe)_{94}Ti_2Al_4$ HEA, in both as-printed and heat-treated states, were studied in terms of nanomechanical behavior in the present work. We firstly investigated the microstructure of this AM-ed HEA, and subsequently studied its nanomechanical behavior including hardness, elastic modulus, and creep behavior in three typical grain orientations. We also discussed the effects of the crystallographic orientation on the mechanical behavior of the AM-ed HEA. Furthermore, the heat treatment effects on the microstructure and nanomechanical behavior of this AM-ed HEA were also revealed. Our research aims to provide a fundamental

understanding of the deformation mechanism of this AM-ed HEA at nanoscale and lead to insights into the internal relation between the microstructure and mechanical properties.

2. Materials and methods

2.1. Specimen fabrication via the LENS^{TM} process

The investigated HEA was polycrystalline with a face-centered-cubic (fcc) structure, and its nominal composition was 23.5 Cr-23.5 Co-23.5 Ni-23.5 Fe-2 Ti-4 Al (at.%). The pre-alloyed powders were prepared by the plasma rotating electrode process (PREP) and were loaded in the powder hopper. Then the powders were blown, via the powder feeding line, to the melt pool, which was established by a high-powered laser beam. The workpiece was moved in the x-y direction to deposit a cross-sectional geometry, and upon a complete layer was deposited, the deposition head was moved upwards (i.e. z-direction, also the build direction) to deposit consecutive layers. To ensure the densification of the HEA specimens, we performed a series of optimization experiments using diverse process parameters. Then the following optimized parameters were used to deposit the HEA specimens: a laser power of 400 W, a laser scan speed of 10 mm/s, and a hatch spacing of 460 μm. Furthermore, the workpiece was scanned in a bi-directional way, and a 90° rotation of the scan direction was adopted when depositing the next layer. Such a scan strategy helped to reduce the residual stress and hence the cracking susceptibility of the specimens. Moreover, to minimize any potential oxidation, the whole deposition process was performed in an argon-purged chamber with an oxygen level below 20 ppm. In order to study the effect of the heat treatment, we performed a direct heat treatment: 650 °C/4 h followed by water quenching.

2.2. Materials characterization

The examined surfaces of the samples (x-z plane) were ground successively up to #4000 emery paper followed by 3 μm and 1 μm diamond paste polishing and electropolishing in H_2SO_4-methanol electrolyte at 24 V for 40 s. To further remove the morphology induced during electropolishing, polishing with 0.25 μm fumed silica suspension (OP-S, Struers) was used as a final step for sample

surface preparation. The roughness of the surface was controlled to a level less than 10 nm in random 10×10 μm^2 areas (see supplementary file). The microstructure and surface morphology of LENS^{TM} manufactured HEA were investigated by scanning electron microscopy (SEM). The SEM (Quanta 650 FEG, ThermoFisher) was operated at 20 kV accelerating voltage, and a solid-state backscattered electron (BSE) detector was used to characterize the microstructure based on the orientation contrast and the atomic number contrast. Electron backscatter diffraction (EBSD) was performed to examine the grain sizes of the two HEA samples and to recognize the distribution of grain orientation. The NORDIF system was used to obtain the EBSD scans. An accelerating voltage of 20 kV at a working distance of ~20 mm was used for the EBSD pattern acquisition. The chemical composition of the particles has been checked by energy-dispersive X-ray spectroscopy (EDS) using a Bruker EDS system in an Ultra 55 SEM (Zeiss) with 10 kV accelerating voltage, ~10 mm working distance and 60 μm aperture.

The nanoindentation tests were carried out on the polished EBSD examined surfaces (also x-z plane) using Hysitron Tribo-indenter TI 950 with a Berkovich indenter tip at ambient temperature. Three typical grain orientations close to {111}, {001} and {101} in the samples were selected for detailed characterization. The detailed procedures for ensuring the indentations performed on these grain orientations are shown in the supplementary material. The nanoindentation characterization was conducted on a load-controlled mode with the maximum loads of 10 mN, and each test ran at the constant loading rate of 0.5 mN/s. The creep properties are studied in the holding stage where the holding time was set as 500 seconds, and thus the creep tests are under constant load. At least 50 indents were performed in the interior of each grain orientation, and a 5 μm indentation spacing was used to avoid the possible effects of the overlapping plastic zones.

3. Results

3.1. Microstructure analysis

The microstructural characteristics of the as-printed and heat-treated HEA observed by electron channeling contrast imaging (ECCI) are shown in Fig.1. Representative ECC images of (a)(c) as-printed sample and (b)(d) heat-treated sample. The theoretical details of this technique can be found in [22]. This is a powerful tool to investigate the microstructure of various metallic materials with a high resolution down to dislocation level [26,27]. The microstructure of the studied HEAs mainly consists of columnar grains, and the layered structure formed during the layer-by-layer deposition process, as shown in Fig.1(a) (b). Furthermore, Fig.1(c) (d) show high-magnification ECC images of the two samples, in which some nano-sized particles can be observed, as shown by the white arrows in the figures. The chemical composition of the particles checked by EDS are shown in Figure S3, which indicates a (Al,Ti)-rich and (Co,Cr,Ni,Fe)-lean composition. In the as-printed specimen, an underlying dislocation cell structure produced during deposition can be observed (polygons indicated by the dashed lines in Fig.1(c)), which is consistent with the results from other AM-ed materials such as austenitic steels [26]. On the contrary, the heat-treated specimen does not show such cells but instead shows densely distributed dislocations in the grain interior (Fig.1 (d)).

The normal direction – inverse pole figure (ND-IPF or IPF-Z) maps in typical areas of the two samples are displayed in Fig.2. The grain size distribution are analyzed in detail, as shown in Fig. R2. The grain size of the heat-treated specimen is slightly smaller than that of the as-printed one in the median, mean and the interquartile range, and therefore the heat treatment in this work does not change the grain size significantly. However, the grains of HEA in both states are much finer than that of the casted HEAs with various compositions (~50 μm) reported in the literature [18,27]. This observation is in line with previous studies that AM methods distinctly refine the microstructure [12,28]. The finer grain size of the AM-ed components can be influenced by several factors, and the most important variable in determining the grain size is attributed to the ultrafast cooling rate during the AM process, which leads

to shorter growth time for the grain [12]. However, the grain size will not has influence on the nanomechanical properties in the following sections, since the indentations are performed in the interior of the grain.

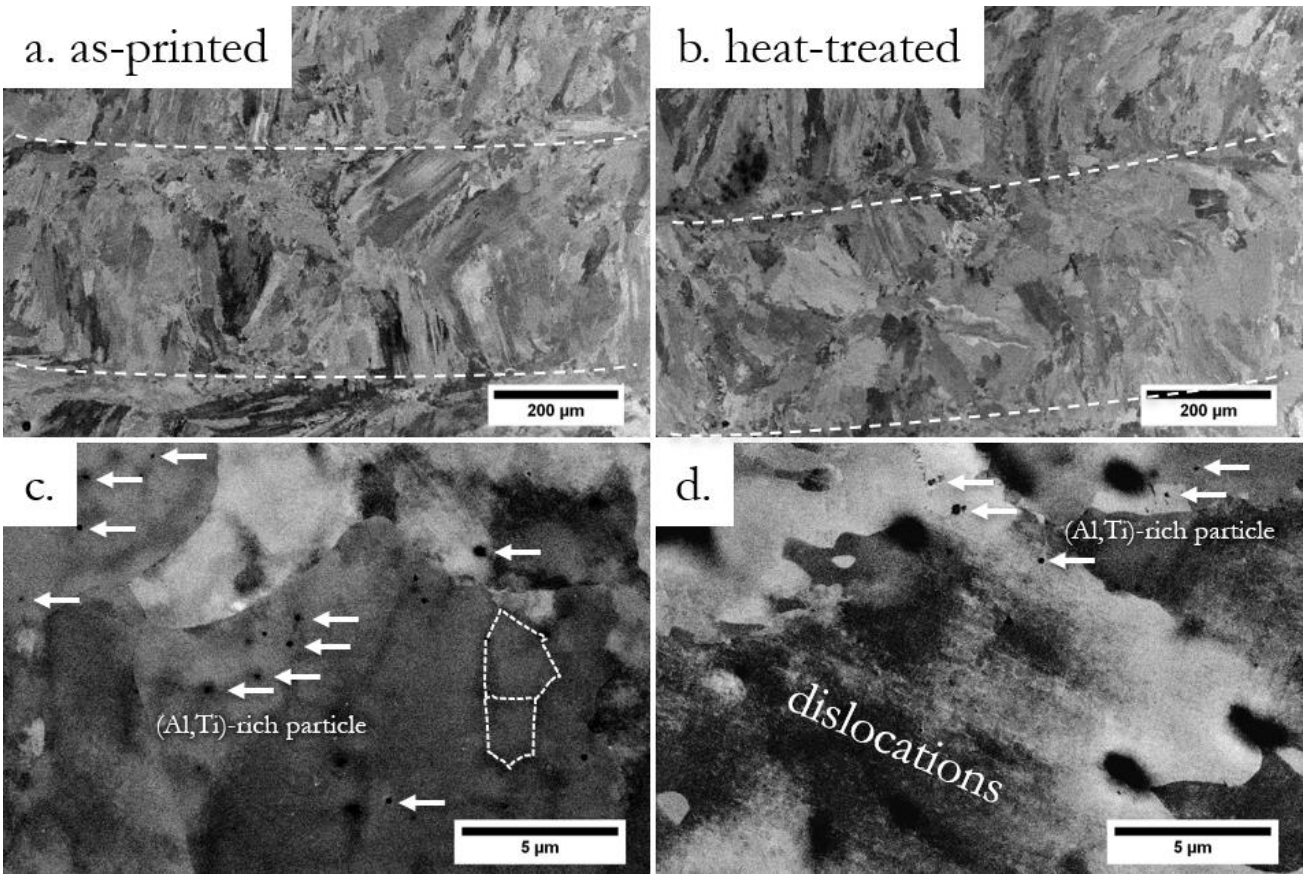

Fig.1. Representative ECC images of (a)(c) as-printed sample and (b)(d) heat-treated sample. The white dash lines in (a)(b) represent the layered structure; the white arrows in (c)(d) show the nano-sized (Al, Ti)-rich particles; the polygons indicated by the dashed lines in (c) represent the underlying dislocation cell structure.

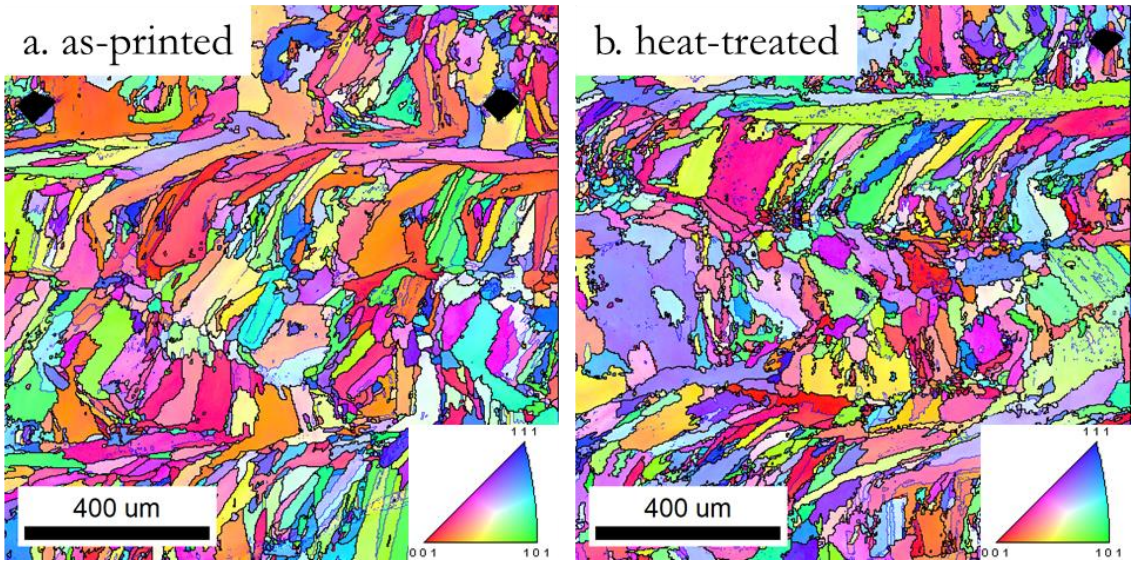

Fig.2. Representative ND-IPF (IPF-Z) maps of (a) as-printed, and (b) heat-treated sample showing the orientation distribution. Building direction upwards. (digital version in color)

3.2. Hardness and elastic modulus

The hardness and elastic modulus of the as-printed and the heat-treated HEA are determined from nanoindentation testing. The used calculation methods were the recognized Oliver and Pharr (O-P) methods [29,30]. The averaged values of the two samples are exhibited in Fig.3. As shown in Fig.3, the hardness values of the two samples for grain orientation {100}, {111}, and {101} are: 2.05±0.16, 2.11±0.12, and 2.20±0.12 GPa for the as-printed sample; 2.76±0.23, 2.83±0.33, and 2.89±0.27 GPa for the heat-treated sample. Compared to the as-printed samples, the hardness of the heat-treated samples increases by 25.7%, 25.4%, 23.9% in the three orientations, respectively. In addition, the elastic modulus of {100}, {111}, and {101} grains were also calculated: 185.97±10.11, 191.85±7.67, and 200.66±7.61 GPa for the as-printed sample; 193.73±11.76, 222.03±21.07, 235.02±20.35 GPa for the heat-treated sample. The elastic modulus increases by 4.0%, 13.6%, 14.6% in the three orientations, respectively. Therefore, both hardness and elastic modulus have the same tendency of grain orientation dependence. The averaged hardness and elastic modulus of {101}-grain are the largest, followed by the {111}-grain and then {001}-grain. These results are inconsistent with previous literature reports [31], in which {111}-grain often exhibits the highest hardness and elastic modulus, and it will be discussed further below. The hardness values of the heat-treated sample are shown to be an average of 25% higher than those of the as-printed sample, which indicates significant strengthening effects of heat treatment on the hardness of the AM-ed HEA. The values of elastic modulus of the heat-treated sample are also relatively larger than those of the as-printed sample with an increasing percentage of 4%-15%, thus the heat treatment also increased elastic modulus to some extent. On the basis of these results, it can be concluded that the heat treatment in this study has a strengthen effect on the hardness and elastic modulus of the AM-ed HEA.

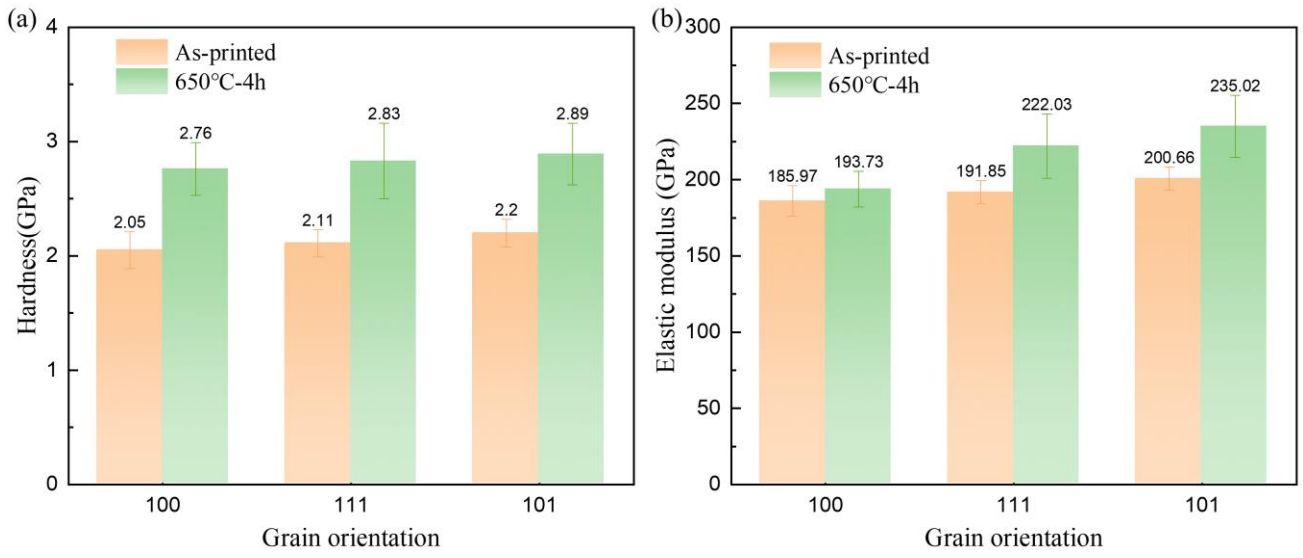

Fig.3. (a) Hardness and (b) Elastic modulus of {100}, {111}, and {101} grains in the as-printed HEA and the heat-treated (650℃-4h) HEA.

3.3. Nanoscale creep behavior at room temperature

Creep is an important plastic property and it is regarded as one of the most important aspects of engineering application. The creep property acts as a critical indicator of component performance, and the research on the creep behavior may lead to a better understanding of the underlying mechanism of their time-dependent plasticity [32]. Nanoscale creep behaviors, besides the hardness and elastic modulus, are also studied in these three grain orientations.

Fig.4a shows the typical load versus displacement curve from the current nanoindentation study, which includes loading, holding, and unloading stages. The creep occurs in the holding stage, and the increase in the penetration depth with holding time was monitored. Then the curves of displacement and strain rate in the holding stage as a function of holding time are plotted in Fig.4b. This creep curve exhibits two stages with different curve slopes: transient creep and steady-state creep. During the transient stage, the displacement increases rapidly with the holding time, and then the increase rate of the creep displacement slows down approaching a constant value, where the creep curve turns to be a steady-state stage. It is noteworthy that, unlike traditional creep, the indentation creep testing does not have a tertiary stage because materials do not thoroughly fail during indentation creep testing.

This creep curve is suggested to be fitted by the commonly used empirical formula [33,34] that was developed for metals:

$$h = h_0 + a(t - t_0)^b + ct \quad (1)$$

where h is the instantaneous indenter depth, h_0 refers to the displacement at the starting of creep, t is time in the holding stage, and t_0, a, b, and c are fitting constants. In addition, t_0 is normally regarded as the beginning time of the creep deformation happens. We rearrange the creep initiation time as the starting point, then t_0 becomes 0 here. As a result, this empirical fitting formula used in this study becomes:

$$h = h_0 + at^b + ct \quad (2)$$

As shown in Fig.4b, the fitting curve as a function of hold time fitted very well and it has a correlation coefficient R^2 of 0.99532.

For depth-sensing indentation creep tests with a self-similar pyramidal indenter, strain rate $\dot{\varepsilon}$ can be estimated by the broadly used equation which was firstly proposed by Mayo and Nix [35,36]:

$$\dot{\varepsilon} = \frac{1}{h}\frac{dh}{dt} \quad (3)$$

The creep strain rate-holding time evolution curve shown in Fig.4b consists of the transient creep stage, where the creep strain rate decreases rapidly with time, and the steady-state creep stage, where the creep strain rate remains almost constant. Specifically, as shown in Fig.4b, during the holding period, the proceeded strain rate of the penetration is relatively high, but the strain rate rapidly decreases with the holding time, and it subsequently reaches the constant creep strain rate at approximately 5×10^{-5} s^{-1} in the steady-state stage. For crystalline materials, the primary creep stage is considered as the viscous behavior related to the dislocation dynamics [37]. The decreasing creep strain rates are proposed to be caused by work hardening effects and enhanced dislocation recovery (rearrangement and annihilation of dislocations), the creep strain rate decreases with time until eventual exhaustion

[38]. As a result, there is a dynamic equilibrium between dislocation generation ($\rho^{\cdot +}$) and annihilation ($\rho^{\cdot -}$) in the steady-state stage, and the final net rate of dislocation generation $\dot{\rho}$ is small for coarse grained metals at ambient temperature [39].

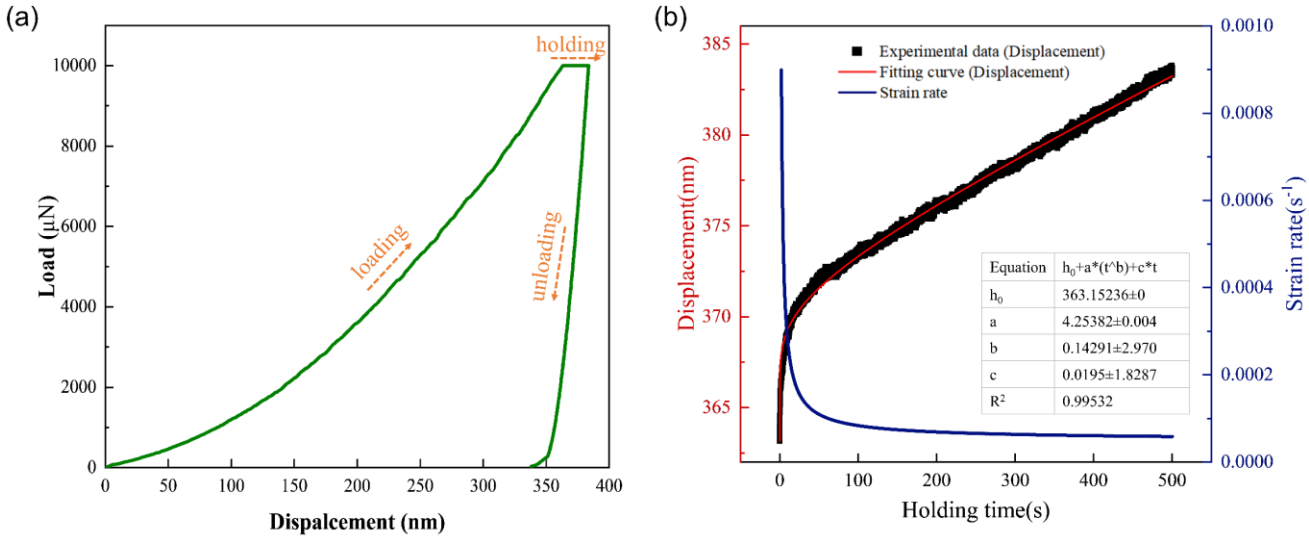

Fig.4. (a) Representative Load-Displacement curve under a constant load of 10 mN, (b) Displacement curve and strain rate in the holding stage as a function of holding time.

According to Tabor's empirical law, the effective stress σ is estimated from instantaneous hardness H as H/C, where C is the constraint factor, which is typically ~3 for metals [40]. The instantaneous hardness is taken as the applied load P divided by the projected contact area A and can be estimated as $P/(24.5h^2)$ for Berkovich indenter, where h is the instantaneous displacement.

During the creep deformation in uniaxial tests, the steady-state creep behavior can be described by the empirical power-law creep equation [36,41,42]:

$$\dot{\varepsilon} = B\sigma^n \exp(-\frac{Q}{RT}) \quad (4)$$

where the pre-coefficient B is a microstructure-dependent constant, Q is the activation energy for creep, n is the creep stress exponent for the steady-state regime, R is the gas constant, and T is the temperature. This equation relates the strain rate to applied stress during the steady-state creep stage. Therefore, the creep stress exponent (n) can be deduced as:

$$n = \frac{\partial ln\dot{\varepsilon}}{\partial ln\sigma} \tag{5}$$

The value of the creep stress exponent can be regarded as an indication of the creep resistance of the metallic materials. To obtain the values of the creep stress exponent, the curves of lnσ-ln$\dot{\varepsilon}$ are plotted. As the representative curve is shown in Fig.5, the slope of the curve decreases with decreasing stress, and the end of the holding period is the steady-state stage where the slope becomes constant, so the creep stress exponent can be obtained by this slope.

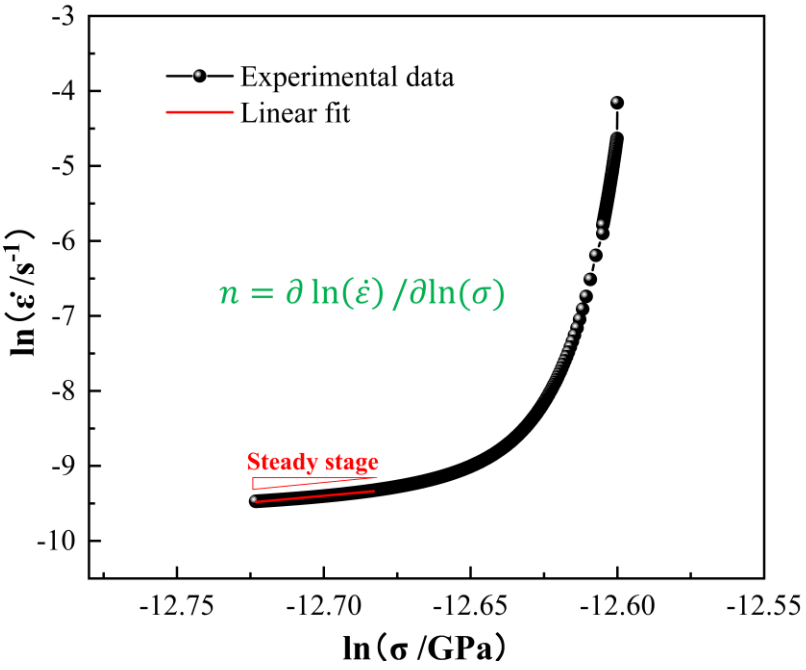

Fig.5. Representative strain rate versus stress curve showing the calculation of creep stress exponent.

Since the microstructures of the AM-ed HEA in this study are non-uniform, at least 50 indents are performed on each grain and most values of *n* fall in the range 0-10. The fitted statistic creep stress exponent distributions of the indentations in {001}, {101}, and {111} grains are plotted in Fig.6. A lognormal distribution model is used to fit the data to better visualize the distributions, and the mode is the most representative value for the lognormal distribution. The mode values of these distributions are summarized in Table 1. The results of the creep stress exponent of the as-printed sample in Fig.6a indicate a great grain orientation anisotropy. The {111}-grain has the largest *n*, followed by {100}, {101}, that is to say, {111}-grain has the highest creep resistance. For the heat-treated sample, the

dependence of creep stress exponent on grain orientation in Fig.6b is not as strong as that of the as-printed sample, but the {111}-grain also has the largest *n*. On the other hand, the values of *n* of the heat-treated sample decrease a little by comparing with that of the as-printed sample, the mode values of the as-printed sample are in the range of 1.54-2.95, while 1.14-1.50 for the heat-treated sample. Moreover, the anisotropy of creep stress exponent of the heat-treated HEA seems to be diminished significantly compared with the as-printed sample, which suggests that the heat treatment can effectively eliminate the nanoscale creep anisotropy. As a whole, although the heat treatment increases the hardness and elastic modulus, it has a slightly negative effect on the creep resistance of the AM-ed HEA. The mechanism behind it will be discussed further later.

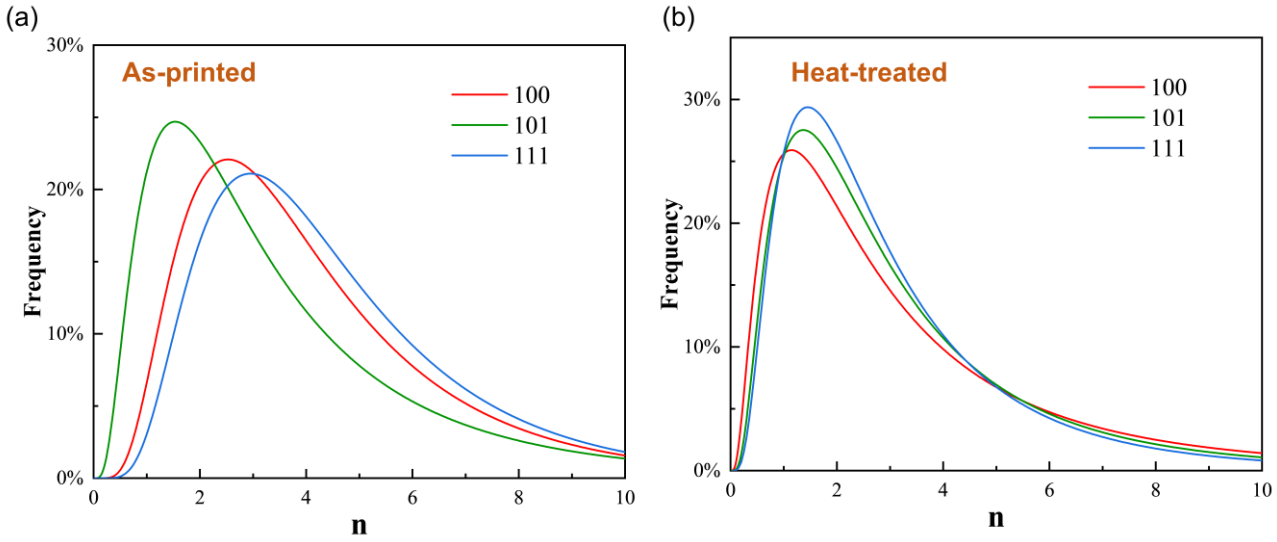

Fig.6. Creep stress exponent distributions of three grain orientations of (a) as-printed HEA and (b) heat-treated HEA.

3.4. Microstructure analysis after deformation

The deformation mechanisms are suggested by correlation with the observation of the microstructure of the deformed surface. Fig.7 shows the typical microstructure after the indentation deformation in a tested {111}-grain of the heat-treated specimen. The wall-like patterns in bright contrast mainly show the solidification structure (i.e. compositional inhomogeneity) from the AM procedure. A note can be given that, to reveal the microstructure for better positioning the indents under an optical microscope,

the topography from electropolishing due to the solidification structure was not further removed. To lessen the topographical influence on the results, multiple indentations were performed to reduce the error and confirm the reproducibility of the results. From Fig.7a, each indent is surrounded by a bright area which can be correlated with the plastic deformation (material pile-up) from the indentation. Fig.7b shows the plastic deformation zone consists of deformation in several different directions in the form of slip bands, as indicated by the dashed lines. In terms of the dislocation slip theory, the dislocations in an FCC lattice are slipping along <110> directions on {111} planes. The observation direction of Fig.7 is <111>, and based on the crystallographic relationship (shown in the bottom-right corner of Fig.7b), the <110> slip traces on this plane will form a triangle that corresponds well with the slip bands observed in Fig.7b, confirming the well-defined slip behavior during the nanoindentation procedure. Furthermore, the slip lines were not intervened by the shape of the Berkovich indent, meaning that the microscale deformation is dominated by the crystallography-controlled slip but not a tip-geometry-controlled process.

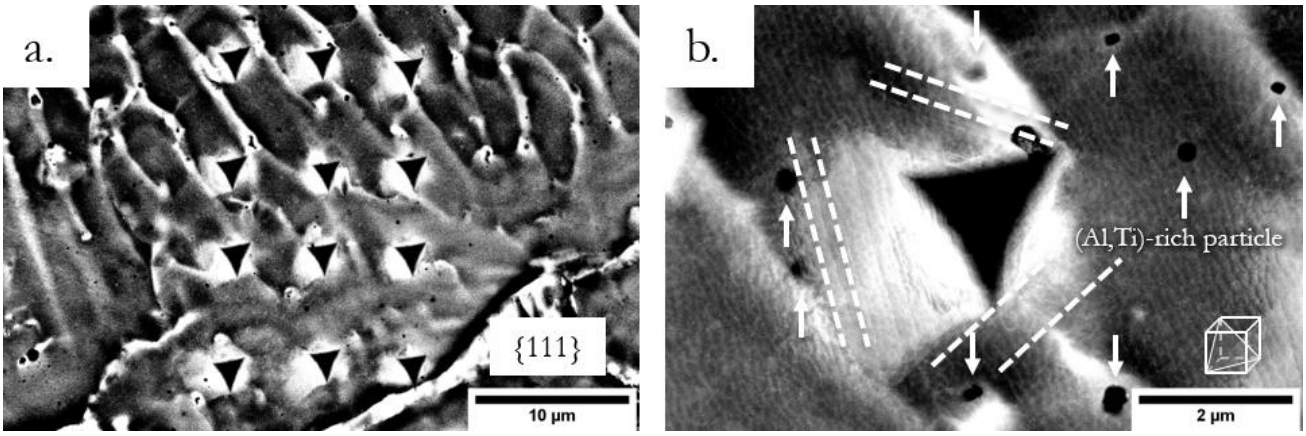

Fig.7. Exemplary ECC images of a tested {111} grain of the heat-treated specimen: (a) overview showing multiple indents; (b) magnified image showing the microstructure in the vicinity of the indent. The dashed lines indicate the slip lines. The white arrows indicate the nanoscale (Al-Ti)-richparticles. The cube in the bottom-right corner shows the investigation plane/ slip plane {111} intersected with the FCC unit cell by the slip directions <110>.

4. Discussion

4.1. Grain orientation dependence

In order to achieve a better understanding of nanoscale elastic-plastic behaviors, as well as optimize the microstructure and nanomechanical properties of the AM-ed HEAs, the investigation of grain orientation dependence is essential.

Hardness represents the measurement of the ability of plastic deformation during nanoindentation. The orientation dependence of the hardness is often explained and studied by the easy-slip model, which gives an insight into the activation of slip and twinning systems from Schmid's law. This model suggests the hardness is in proportion to the reciprocal of the maximum Schmid factor [43]. The minimal stress value (σ_{min}) under the indenter for initiating the slips is determined by the critical resolved shear stress (CRSS) which is a constant of crystal material, and the corresponding formula is:

$$\sigma_{min} = \frac{\tau_{CRSS}}{S_{max}} \tag{6}$$

where τ_{CRSS} is the critical resolved shear stress (CRSS), and it is the minimum shear stress required for a slip to happen; S_{max} is the maximum Schmid factor. Compared to the uniaxial deformation condition, the stress state of nanoindentation is more complicated. The stress σ under the indenter is related to the hardness in the following form:

$$\sigma = \frac{H \times A_c}{A} \tag{7}$$

where A_c is the contact area, A is the projected area.

The hardness, therefore, can be associated with the Schmid factor. The calculation of the Schmid factor is dependent on the slip system at a specific crystal position. Previous studies have investigated the maximum Schmid factors for fcc slip and twinning systems under compressions along with the directions of <111>, <101>, and <100>, where the Schmid factors along <111> are the lowest, indicating the highest hardness, <100> has the largest Schmid factor thus <100> are regarded as the

soft orientation [31,44]. However, this is not consistent with our experimental results that {101}-grain has the largest hardness. It should be pointed out that, twinning, as a deformation mechanism, was not observed visibly in this material according to the SEM micrographs, thus the slip systems dominated this model in the current work. To explain this interesting finding, we might consider that Schmid's law is a simple approximate law, and it is based on the basic assumption that the material is defect-free so that the deformation behavior is only dominated by dislocation slipping. Nevertheless, in the two samples of the current work, the dislocation density and defect density are deemed to be enhanced by the AM process, thus the impact of dislocation and defects should not be ignored. It is suggested that the measured hardness of different orientations can also be affected by the dislocation density and the associated dislocation nucleation and emission on the {111}, {101}, and {100} planes [44]. Furthermore, a previous study has proposed that the {111}-grain is more sensitive to the influence of defects and less sensitive to the influence of crystallography, while {100}-grain is less sensitive to the influence of defects [45]. Therefore, the AM method might cause the change of dislocation density in different orientations, which can contribute to the associated finding. Besides, it is clear that the hardness showed the orientation dependence in the current work, but the dependency is not very strong. The dislocation nucleation and the maximum shear stress for initiate plasticity in one HEA have also been found to be insensitive to the crystallographic orientation [46]. An alternative explanation for this trend is that the fcc structure of HEAs is relatively different from that of traditional fcc metals and alloys, and it is a distorted lattice structure due to the different atomic sizes of the elements. The sluggish diffusion effect of the multiple dominant elements and the lattice-strain effect are present in HEAs, which could lead to different deformation behavior under similar conditions [6].

The orientation dependence of the elastic modulus can be attributed to the anisotropy independent compliances of a cubic crystal system [31,47,48]. It is suggested that the anisotropy of the elastic modulus (E_{hkl}) is dependent on an anisotropy factor A_{hkl}, which is defined as:

$$A_{h\,k\,l} = \frac{h^2k^2+k^2l^2+l^2k^2}{(h^2+k^2+l^2)^2} \quad (8)$$

where *h*, *k*, *l* are the Miller indices obtained by Euler's angles. As a consequence, $A_{1\,0\,0}$ is equal to 0, $A_{1\,1\,0}$ is 1/4, and $A_{1\,1\,1}$ is 1/3. Subsequently, the anisotropy dependence of the elastic modulus ($E_{h\,k\,l}$) is given by:

$$\frac{1}{E_{h\,k\,l}} = S_{11} + (2S_{12} - 2S_{11} + S_{44})A_{h\,k\,l} \quad (9)$$

where S_{11}, S_{12}, and S_{44} are the anisotropy compliances of the tested material. Since the HEA used in this work is a novel type of HEAs, there is no corresponding literature to calculate the compliances for the time being. Further investigation and prediction, therefore, are required to elucidate the anisotropy compliances of this kind of HEAs, which might be used to give a rational explanation to this finding. Moreover, lattice distortion, as a crucial characteristic of HEAs, may lead to heterogeneous local lattice strain that is attributed to incommensurate elasticity. In a recent study, the effect of electron density inconsistency in HEAs was discovered to play a primary role in the anisotropic elasticity, and the elastic anisotropy of HEA is relatively low in their calculation [49].

Considering the orientation dependency of the creep deformation, {111}-grain had the greatest creep resistance. As will be shown later, the creep mechanism of the HEA in both states is likely to be lattice diffusion dominant, so the easy-slip model would not applicable anymore for rationalizing the orientation-dependent creep behavior. Nevertheless, so far, there are few studies devoted to the mechanism behind it. Further efforts are required to understand the mechanism and clarify this novel finding, a detailed investigation for the mechanism behind the results is beyond the scope of the current work.

4.2. Nanoscale creep behavior and creep mechanism of AM-ed HEA

By comparing previous studies on the nanoindentation creep behavior of HEAs [27,50–52], the values of the creep stress exponent extracted in this work are much smaller, which means the nanoscale creep

resistance of AM-ed HEAs is not comparable to that of conventional HEAs. Owing to the inherent nature of HEAs involving sluggish atom diffusion and severe lattice distortion, the movement of the dislocations in the HEAs can be retarded readily [37], the creep resistance can be therefore enhanced exactly as many HEAs have been reported that have outstanding creep resistance. Nevertheless, the AM method usually causes high dislocation density, which decreases the creep resistance. Therefore, the constraints of the creep behavior of AM-ed HEAs can be a trade-off, and the relatively inferior creep resistance of the AM-ed HEA specimens might be attributed to the high dislocation density.

It is crucial to estimate the principal creep mechanism for better understanding the time-dependent viscoplasticity of HEAs at the nanoscale. Creep stress exponent (n) is regarded as one of the useful indicators for estimating the predominant creep mechanism. It has been well accepted in the conventional creep tests and most indentation creep tests have been using this as the indicator although there is controversy about it for the time being. For estimating the creep mechanism by this indicator, n=1 for diffusion creep, such as Coble creep by grain boundary (GB) diffusion and Nabarro-Herring creep by lattice diffusion, n=2 for GB sliding, and n=3–8 for dislocation creep, n>10 for the dislocation-precipitate interaction creep [53].

What is noteworthy is that the nanoindentation creep is performed in the interior of each grain and at a very small volume, namely, the size of the indentation contact is much smaller than the grain size. Therefore, the creep process can be hardly influenced by grain boundary, in this case, grain boundary sliding or Coble diffusional creep processes existing in the bulk may not be considered. In this study, the results of the two samples show that the value of n varies from 1-3. So here for nanoindentation creep, the dominant creep mechanism for the AM-ed HEA is likely to be Nabarro-Herring creep by lattice diffusion.

The thermal activation volume is another essential indicator for understanding the creep mechanism because the creep deformation is a thermally activated process [54]. The apparent activated volume

V^* represents the physical volume involved in plastic deformation, the applied stress acts on this volume, helping to deform by reducing the energy barrier [55]. The thermal apparent activation volume V^* is estimated by this equation [56]:

$$V^* = MkT\left(\frac{\partial ln\dot{\varepsilon}}{\partial\sigma}\right) = \frac{\sqrt{3}nkT}{\sigma} \quad (10)$$

where M is the Taylor factor estimated with von Mises relation (M=$\sqrt{3}$), k is Boltzmann's constant, and T is the temperature in Kelvin. The apparent activation volume should be obtained at the steady-state creep stage in order to avoid any microstructure change due to work hardening [57].

Different deformation mechanisms usually involve specific activation volumes. In fcc metals, the diffusion creep (lattice or GB diffusion) or dislocation climb becomes the dominate mechanism when V^*~b^3; for V^*=10b^3-100b^3, the creep mechanism is Cross-slip; when V^*=100b^3-1000b^3, the dislocation glide is the controlling mechanism [18,55,58].

By employing the representative n from 'mode' data points, the V^* is calculated and normalized to the cube of Burgers vector, the Burgers vector b for HEA is b=0.25 nm [18]. The results of the activation volume are summarized in Table 1. The values for different orientations of two samples become the same tendency, that is, {111}-grain shows the largest activation volume, the following is {100}-grain, then is {101}-grain, so {111}-grain shows the greatest creep resistance. However, all of the values of activation volume are around 1b^3, which indicates the diffusion mechanism is likely to be the controlling creep mechanism. This is in agreement with the estimated values of n in this study, which indicate the same dominant creep deformation mechanism. It was proposed by Wang et al. [59] that tip-sample interfacial diffusion could be the dominant creep mechanism for relatively shallow indentation (the critical indentation depth is ~12 nm), whereas when indentation depth becomes deeper, the interfacial diffusion effects could be neglected so that conventional creep mechanisms related to microstructural activities will dominate the creep mechanism. In this work, the indentation depths are

all larger than 300 nm, which are deep enough to neglect the interfacial diffusion, so the creep mechanism of HEA in the current case is lattice diffusion.

Table 1. Creep stress exponent and activation volume of different grain orientation

Sample	**Grain orientation**	**Creep stress exponent (*n*)**	**Activation volume (*V**)**
As-printed	{100}	2.52	$1.68b^3$
	{101}	1.54	$1.02b^3$
	{111}	2.95	$2.15b^3$
650℃-4h	{100}	1.14	$0.81b^3$
	{101}	1.41	$0.71b^3$
	{111}	1.50	$1.06b^3$

4.3. The effect of heat treatment

In AM, post-process heat treatment has been widely investigated to remove residual stress caused by complex thermal history, and meanwhile, improve the comprehensive mechanical properties [60], thus it is important for further industrial applications.

In this work, the heat treatment at 650℃ for 4 hours has been found to have an obvious effect on the nanomechanical properties of AM-ed HEA. To be specific, the hardness and elastic modulus of the heat-treated HEA increase to some extent. One possible mechanisms may account for this finding, which is due to the existence of the short range ordered (SRO) domains in the HEAs. Evidence from other studies suggests that SRO domains of the HEAs have a great influence on the dislocation mediated plasticity by increasing the activation energy barrier, which will further reinforce the effect of solid solution strengthening [61–63]. In addition, studies have shown that the heat treatment could

increase the degree of SRO domains and in turn induce the strengthening effect [63,64]. Therefore, the increasing hardness of the heat-treated sample can be explained by this mechanism.

On the other side, for the heat-treated sample, there is a slight reduction in the creep resistance at the nanoscale in comparison with the as-printed sample, which is the opposite trend of the hardness and elastic modulus results. Moreover, the anisotropy of creep behavior of the heat-treated HEA reduced significantly than that of as-printed HEA, which means the heat treatment, could eliminate the nanoscale creep anisotropy. This is an interesting finding, as several studies have found that applying heat treatment could improve the creep resistance of AM-ed alloys by conventional creep testing [65–67], the reasons for which remain unclear currently. However, there is a recent study reporting that the creep rate of the aged sample is faster than the non-aged sample, which suggests the precipitation affected by the heat treatment could effectively block the mobile dislocations and then increase the creep rate [68]. So far, little evidence is available for the reason how heat treatment influences the nanoscale creep behavior, and this issue is considered as a potential area for further study.

5. Conclusion

By aid of nanoindentation and SEM, the microstructure and orientation-dependent nanomechanical behaviors of an AM-ed $(CrCoNiFe)_{94}Ti_2Al_4$ HEA were systematically investigated in the current work. Furthermore, two states of HEA including as-printed and heat-treated were used to study the effect of heat treatment in AM. The fundamental understanding of the unique mechanical properties and the creep deformation mechanism of AM-ed HEA at the nanoscale were consequently afforded. The major results are summarized as follows.

1. The microstructure of the studied AM-ed HEA mainly consists of columnar grains, and some nano-sized precipitates can be observed. Both as-printed and heat-treated HEA show finer grain size than the casted HEAs, which is attributed to the ultrafast cooling rate during the AM process.

2. Both hardness and elastic modulus of HEA in two states have the same tendency of orientation dependence, that is, {101}>{111}>{100}. Furthermore, the creep resistance of the two samples shows different orientation dependencies, and {111}-grain has the highest creep stress exponent for both samples indicating the highest creep resistance. This interesting trend brings to light the potential distinctive mechanism responsible for the orientation dependence of the AM-ed HEAs.

3. The values of the creep stress exponent are in the range of 1-3. Evaluation of the creep stress exponent and the activation volume suggests that the controlling creep mechanism of AM-ed HEA in the present study is the Nabarro-Herring creep by lattice diffusion.

4. Heat treatment of AM-ed HEA in the current case can increase the hardness and elastic modulus, but decrease the creep resistance slightly and eliminate the nanoscale creep anisotropy.

Insights into these results are expected to contribute to a better understanding of the characteristic nanomechanical properties of AM-ed HEAs, and therefore be a reference for further optimization of material design and manufacturing process for potential applications.

CRediT authorship contribution statement

Siqi Liu: Conceptualization, Methodology, Investigation, Writing – original draft, Writing – review & editing, Formal analysis, Visualization, Validation. **Di Wan:** Formal analysis, Investigation, Validation, Writing - Review & Editing. **Shuai Guan:** Resources, Writing - Review & Editing. **Yuequn Fu:** Writing - Review & Editing, Formal analysis. **Xiaobo Ren:** Writing - Review & Editing. **Zhiliang Zhang:** Writing - Review & Editing, Supervision. **Jianying He:** Validation, Writing - Review & Editing, Supervision, Funding acquisition.

Declaration of competing interest

There are no conflicts to declare.

Acknowledgments

The Research Council of Norway (Grant No. 251068) and the Chinese Scholarship Council are acknowledged for the support of this work.

Reference

[1] B. Cantor, I.T.H. Chang, P. Knight, A.J.B. Vincent, Microstructural development in equiatomic multicomponent alloys, Mater. Sci. Eng. A. 375–377 (2004) 213–218. https://doi.org/10.1016/j.msea.2003.10.257.

[2] W. Zhang, P.K. Liaw, Y. Zhang, Science and technology in high-entropy alloys, Sci. China Mater. 61 (2018) 2–22. https://doi.org/10.1007/s40843-017-9195-8.

[3] E.P. George, D. Raabe, R.O. Ritchie, High-entropy alloys, Nat. Rev. Mater. 4 (2019) 515–534. https://doi.org/10.1038/s41578-019-0121-4.

[4] B. Gludovatz, A. Hohenwarter, D. Catoor, E.H. Chang, E.P. George, R.O. Ritchie, A fracture-resistant high-entropy alloy for cryogenic applications, Science (80-.). 345 (2014) 1153–1158. https://doi.org/10.1126/science.1254581.

[5] S. Maiti, W. Steurer, Structural-disorder and its effect on mechanical properties in single-phase TaNbHfZr high-entropy alloy, Acta Mater. 106 (2016) 87–97. https://doi.org/10.1016/j.actamat.2016.01.018.

[6] Z. Li, S. Zhao, R.O. Ritchie, M.A. Meyers, Mechanical properties of high-entropy alloys with emphasis on face-centered cubic alloys, Prog. Mater. Sci. 102 (2019) 296–345. https://doi.org/10.1016/j.pmatsci.2018.12.003.

[7] J.Y. He, H. Wang, H.L. Huang, X.D. Xu, M.W. Chen, Y. Wu, X.J. Liu, T.G. Nieh, K. An, Z.P. Lu, A precipitation-hardened high-entropy alloy with outstanding tensile properties, Acta Mater. 102 (2016) 187–196. https://doi.org/10.1016/j.actamat.2015.08.076.

[8] W.H. Liu, T. Yang, C.T. Liu, Precipitation hardening in CoCrFeNi-based high entropy alloys, Mater. Chem. Phys. 210 (2018) 2–11. https://doi.org/10.1016/j.matchemphys.2017.07.037.

[9] S.A. Adekanye, R.M. Mahamood, E.T. Akinlabi, M.G. Owolabi, Additive manufacturing: The future of manufacturing: Dodajalna (3D) Tehnologija: Prihodnost Proizvajanja, Mater. Tehnol. 51 (2017) 709–715. https://doi.org/10.17222/mit.2016.261.

[10] M. Li, T. Lu, J. Dai, X. Jia, X. Gu, T. Dai, Microstructure and mechanical properties of 308L stainless steel fabricated by laminar plasma additive manufacturing, Mater. Sci. Eng. A. 770 (2020). https://doi.org/10.1016/j.msea.2019.138523.

[11] W.E. Frazier, Metal additive manufacturing: A review, J. Mater. Eng. Perform. 23 (2014) 1917–1928. https://doi.org/10.1007/s11665-014-0958-z.

[12] T. DebRoy, H.L. Wei, J.S. Zuback, T. Mukherjee, J.W. Elmer, J.O. Milewski, A.M. Beese, A. Wilson-Heid, A. De, W. Zhang, Additive manufacturing of metallic components – Process, structure and properties, Prog. Mater. Sci. 92 (2018) 112–224. https://doi.org/10.1016/j.pmatsci.2017.10.001.

[13] S. Gorsse, C. Hutchinson, M. Gouné, R. Banerjee, Additive manufacturing of metals: a brief review of the characteristic microstructures and properties of steels, Ti-6Al-4V and high-entropy alloys, Sci. Technol. Adv. Mater. 18 (2017) 584–610. https://doi.org/10.1080/14686996.2017.1361305.

[14] N. Yang, J. Yee, B. Zheng, K. Gaiser, T. Reynolds, L. Clemon, W.Y. Lu, J.M. Schoenung, E.J. Lavernia, Process-Structure-Property Relationships for 316L Stainless Steel Fabricated by Additive Manufacturing and Its Implication for Component Engineering, J. Therm. Spray Technol. 26 (2017) 610–626. https://doi.org/10.1007/s11666-016-0480-y.

[15] S. Guan, K. Solberg, D. Wan, F. Berto, T. Welo, T.M. Yue, K.C. Chan, Formation of fully equiaxed grain microstructure in additively manufactured AlCoCrFeNiTi0.5 high entropy alloy, Mater. Des. 184 (2019) 108202. https://doi.org/10.1016/j.matdes.2019.108202.

[16] Z.Y. Ding, B.X. Cao, J.H. Luan, Z.B. Jiao, Synergistic effects of Al and Ti on the oxidation behaviour and mechanical properties of L12-strengthened FeCoCrNi high-entropy alloys, Corros. Sci. 184 (2021) 109365. https://doi.org/10.1016/j.corsci.2021.109365.

[17] Y. Ma, G.J. Peng, D.H. Wen, T.H. Zhang, Nanoindentation creep behavior in a CoCrFeCuNi high-entropy alloy film with two different structure states, Mater. Sci. Eng. A. 621 (2015) 111–117. https://doi.org/10.1016/j.msea.2014.10.065.

[18] D.H. Lee, M.Y. Seok, Y. Zhao, I.C. Choi, J. He, Z. Lu, J.Y. Suh, U. Ramamurty, M. Kawasaki, T.G. Langdon, J. Il Jang, Spherical nanoindentation creep behavior of nanocrystalline and coarse-grained CoCrFeMnNi high-entropy alloys, Acta Mater. 109 (2016) 314–322. https://doi.org/10.1016/j.actamat.2016.02.049.

[19] J.J. Lewandowski, M. Seifi, Metal Additive Manufacturing: A Review of Mechanical Properties, Annu. Rev. Mater. Res. 46 (2016) 151–186. https://doi.org/10.1146/annurev-matsci-070115-032024.

[20] W.B. Li, J.L. Henshall, R.M. Hooper, K.E. Easterling, The mechanisms of indentation creep, Acta Metall. Mater. 39 (1991) 3099–3110. https://doi.org/10.1016/0956-7151(91)90043-Z.

[21] M. Muhammad, M. Masoomi, B. Torries, N. Shamsaei, M. Haghshenas, Depth-sensing time-dependent response of additively manufactured Ti-6Al-4V alloy, Addit. Manuf. 24 (2018) 37–46. https://doi.org/10.1016/j.addma.2018.09.008.

[22] S. Zaefferer, N.N. Elhami, Theory and application of electron channelling contrast imaging under controlled diffraction conditions, Acta Mater. 75 (2014) 20–50. https://doi.org/10.1016/j.actamat.2014.04.018.

[23] S. Guan, D. Wan, K. Solberg, F. Berto, T. Welo, T.M. Yue, K.C. Chan, Additively manufactured CrMnFeCoNi/AlCoCrFeNiTi0.5 laminated high-entropy alloy with enhanced strength-plasticity synergy, Scr. Mater. 183 (2020) 133–138. https://doi.org/10.1016/j.scriptamat.2020.03.032.

[24] S. Guan, D. Wan, K. Solberg, F. Berto, T. Welo, T.M. Yue, K.C. Chan, Additive manufacturing of fine-grained and dislocation-populated CrMnFeCoNi high entropy alloy by laser engineered net shaping, Mater. Sci. Eng. A. 761 (2019) 138056. https://doi.org/10.1016/j.msea.2019.138056.

[25] D. Wan, A. Barnoush, Plasticity in cryogenic brittle fracture of ferritic steels: Dislocation versus twinning, Mater. Sci. Eng. A. 744 (2019) 335–339. https://doi.org/10.1016/j.msea.2018.12.038.

[26] K.M. Bertsch, G. Meric de Bellefon, B. Kuehl, D.J. Thoma, Origin of dislocation structures in an additively manufactured austenitic stainless steel 316L, Acta Mater. 199 (2020) 19–33. https://doi.org/10.1016/j.actamat.2020.07.063.

[27] M.T. Tsai, J.C. Huang, P.H. Lin, T.Y. Liu, Y.C. Liao, J.S.C. Jang, S.X. Song, T.G. Nieh, Creep of face-centered-cubic {111} and {100} grains in FeCoNiCrMn and FeCoNiCrMn–Al alloys: Orientation and solid solution effects, Intermetallics. 103 (2018) 88–96. https://doi.org/10.1016/j.intermet.2018.10.006.

[28] D. Herzog, V. Seyda, E. Wycisk, C. Emmelmann, Additive manufacturing of metals, Acta

Mater. 117 (2016) 371–392. https://doi.org/10.1016/j.actamat.2016.07.019.

[29] W.C. Oliver, G.M. Pharr, An improved technique for determining hardness and elastic modulus using load and displacement sensing indentation experiments, J. Mater. Res. 7 (1992) 1564–1583. https://doi.org/10.1557/jmr.1992.1564.

[30] W.C. Oliver, G.M. Pharr, Measurement of hardness and elastic modulus by instrumented indentation: Advances in understanding and refinements to methodology, J. Mater. Res. 19 (2004) 3–20. https://doi.org/10.1557/jmr.2004.19.1.3.

[31] T. Chen, L. Tan, Z. Lu, H. Xu, The effect of grain orientation on nanoindentation behavior of model austenitic alloy Fe-20Cr-25Ni, Acta Mater. 138 (2017) 83–91. https://doi.org/10.1016/j.actamat.2017.07.028.

[32] A.C. Fischer-Cripps, A simple phenomenological approach to nanoindentation creep, Mater. Sci. Eng. A. 385 (2004) 74–82. https://doi.org/10.1016/j.msea.2004.04.070.

[33] S.-M. Chen, H.-L. Gao, X.-H. Sun, Z.-Y. Ma, T. Ma, J. Xia, Y.-B. Zhu, R. Zhao, H.-B. Yao, H.-A. Wu, S.-H. Yu, Superior Biomimetic Nacreous Bulk Nanocomposites by a Multiscale Soft-Rigid Dual-Network Interfacial Design Strategy, Matter. 1 (2019) 412–427. https://doi.org/10.1016/j.matt.2019.03.012.

[34] H. Li, A.H.W. Ngan, Size effects of nanoindentation creep, J. Mater. Res. 19 (2004) 513–522. https://doi.org/10.1557/jmr.2004.0063.

[35] M.J. Mayo, W.D. Nix, A micro-indentation study of superplasticity in Pb, Sn, and Sn-38 wt% Pb, Acta Metall. 36 (1988) 2183–2192. https://doi.org/10.1016/0001-6160(88)90319-7.

[36] R. Goodall, T.W. Clyne, A critical appraisal of the extraction of creep parameters from nanoindentation data obtained at room temperature, Acta Mater. 54 (2006) 5489–5499. https://doi.org/10.1016/j.actamat.2006.07.020.

[37] S. Chen, W. Li, X. Xie, J. Brechtl, B. Chen, P. Li, G. Zhao, F. Yang, J. Qiao, K.A. Dahmen, P.K. Liaw, Nanoscale serration and creep characteristics of Al0.5CoCrCuFeNi high-entropy alloys, J. Alloys Compd. 752 (2018) 464–475. https://doi.org/10.1016/j.jallcom.2018.04.137.

[38] M. Haghshenas, Y. Wang, Y.T. Cheng, M. Gupta, Indentation-based rate-dependent plastic deformation of polycrystalline pure magnesium, Mater. Sci. Eng. A. 716 (2018) 63–71. https://doi.org/10.1016/j.msea.2018.01.036.

[39] J. Hu, W. Zhang, G. Bi, J. Lu, W. Huo, Y. Zhang, Nanoindentation creep behavior of coarse-grained and ultrafine-grained pure magnesium and AZ31 alloy, Mater. Sci. Eng. A. 698 (2017) 348–355. https://doi.org/10.1016/j.msea.2017.05.063.

[40] I.C. Choi, B.G. Yoo, Y.J. Kim, M.Y. Seok, Y. Wang, J. Il Jang, Estimating the stress exponent of nanocrystalline nickel: Sharp vs. spherical indentation, Scr. Mater. 65 (2011) 300–303. https://doi.org/10.1016/j.scriptamat.2011.04.031.

[41] W.B. Li, J.L. Henshall, R.M. Hooper, K.E. Easterling, The mechanisms of indentation creep, Acta Metall. Mater. 39 (1991) 3099–3110. https://doi.org/10.1016/0956-7151(91)90043-Z.

[42] R. Berriche, An investigation of the creep processes in tin and aluminum using a depth-sensing indentation technique, J. Mater. Res. 7 (1992) 627–638. https://doi.org/10.1557/JMR.1992.0627.

[43] T. Csanádi, M. Bl'Anda, N.Q. Chinh, P. Hvizdoš, J. Dusza, Orientation-dependent hardness and nanoindentation-induced deformation mechanisms of WC crystals, Acta Mater. 83 (2015) 397–407. https://doi.org/10.1016/j.actamat.2014.09.048.

[44] K.S. Mao, C. Sun, Y. Huang, C.H. Shiau, F.A. Garner, P.D. Freyer, J.P. Wharry, Grain orientation dependence of nanoindentation and deformation-induced martensitic phase transformation in neutron irradiated AISI 304L stainless steel, Materialia. 5 (2019) 100208. https://doi.org/10.1016/j.mtla.2019.100208.

[45] S.K. Lawrence, D.F. Bahr, H.M. Zbib, Crystallographic orientation and indenter radius effects on the onset of plasticity during nanoindentation, J. Mater. Res. 27 (2012) 3058–3065. https://doi.org/10.1557/jmr.2012.368.

[46] C. Zhu, Z.P. Lu, T.G. Nieh, Incipient plasticity and dislocation nucleation of FeCoCrNiMn high-entropy alloy, Acta Mater. 61 (2013) 2993–3001. https://doi.org/10.1016/j.actamat.2013.01.059.

[47] S. Kang, Y.S. Jung, B.G. Yoo, J. il Jang, Y.K. Lee, Orientation-dependent indentation modulus and yielding in a high Mn twinning-induced plasticity steel, Mater. Sci. Eng. A. 532 (2012) 500–504. https://doi.org/10.1016/j.msea.2011.10.116.

[48] J.C. Stinville, C. Tromas, P. Villechaise, C. Templier, Anisotropy changes in hardness and indentation modulus induced by plasma nitriding of 316L polycrystalline stainless steel, Scr. Mater. 64 (2011) 37–40. https://doi.org/10.1016/j.scriptamat.2010.08.058.

[49] C.C. Yen, G.R. Huang, Y.C. Tan, H.W. Yeh, D.J. Luo, K.T. Hsieh, E.W. Huang, J.W. Yeh, S.J. Lin, C.C. Wang, C.L. Kuo, S.Y. Chang, Y.C. Lo, Lattice distortion effect on elastic anisotropy of high entropy alloys, J. Alloys Compd. 818 (2020) 152876. https://doi.org/10.1016/j.jallcom.2019.152876.

[50] P.F. Zhou, D.H. Xiao, G. Li, M. Song, Nanoindentation Creep Behavior of CoCrFeNiMn High-Entropy Alloy under Different High-Pressure Torsion Deformations, J. Mater. Eng. Perform. 28 (2019) 2620–2629. https://doi.org/10.1007/s11665-019-04092-1.

[51] L. Zhang, P. Yu, H.U. Cheng, H. Zhang, H. Diao, Y. Shi, B. Chen, P. Chen, R. Feng, J. Bai, Q. Jing, M. Ma, P.K. Liaw, G. Li, R. Liu, Nanoindentation Creep Behavior of an Al 0.3 CoCrFeNi High-Entropy Alloy, Metall. Mater. Trans. A. 47 (n.d.). https://doi.org/10.1007/s11661-016-3469-8.

[52] Y. Ma, Y.H. Feng, T.T. Debela, G.J. Peng, T.H. Zhang, Nanoindentation study on the creep characteristics of high-entropy alloy films: fcc versus bcc structures, Int. J. Refract. Met. Hard Mater. 54 (2016) 395–400. https://doi.org/10.1016/j.ijrmhm.2015.08.010.

[53] P. Yavari, T.G. Langdon, An examination of the breakdown in creep by viscous glide in solid solution alloys at high stress levels, Acta Metall. 30 (1982) 2181–2196. https://doi.org/10.1016/0001-6160(82)90139-0.

[54] I.C. Choi, Y.J. Kim, M.Y. Seok, B.G. Yoo, J.Y. Kim, Y. Wang, J. Il Jang, Nanoscale room temperature creep of nanocrystalline nickel pillars at low stresses, Int. J. Plast. 41 (2013) 53–64. https://doi.org/10.1016/j.ijplas.2012.08.008.

[55] M.A. Monclús, J.M. Molina-Aldareguia, High Temperature Nanomechanical Testing, in: Handb. Mech. Mater., 2018: pp. 1–29. https://doi.org/10.1007/978-981-10-6855-3_55-1.

[56] J. Xu, H. Gruber, D. Deng, R.L. Peng, J.J. Moverare, Short-term creep behavior of an additive manufactured non-weldable Nickel-base superalloy evaluated by slow strain rate testing, Acta Mater. 179 (2019) 142–157. https://doi.org/10.1016/j.actamat.2019.08.034.

[57] H. Wang, A. Dhiman, H.E. Ostergaard, Y. Zhang, T. Siegmund, J.J. Kruzic, V. Tomar, Nanoindentation based properties of Inconel 718 at elevated temperatures: A comparison of conventional versus additively manufactured samples, Int. J. Plast. 120 (2019) 380–394. https://doi.org/10.1016/j.ijplas.2019.04.018.

[58] Y.J. Kim, W.W. Lee, I.C. Choi, B.G. Yoo, S.M. Han, H.G. Park, W. Il Park, J. Il Jang, Time-

dependent nanoscale plasticity of ZnO nanorods, Acta Mater. 61 (2013) 7180–7188. https://doi.org/10.1016/j.actamat.2013.08.022.

[59] F. Wang, P. Huang, T. Lu, Surface-effect territory in small volume creep deformation, J. Mater. Res. 24 (2009) 3277–3285. https://doi.org/10.1557/jmr.2009.0416.

[60] L. Zhuo, Z. Wang, H. Zhang, E. Yin, Y. Wang, T. Xu, C. Li, Effect of post-process heat treatment on microstructure and properties of selective laser melted AlSi10Mg alloy, Mater. Lett. 234 (2019) 196–200. https://doi.org/10.1016/j.matlet.2018.09.109.

[61] E. Antillon, C. Woodward, S.I. Rao, B. Akdim, T.A. Parthasarathy, Chemical short range order strengthening in a model FCC high entropy alloy, Acta Mater. 190 (2020) 29–42. https://doi.org/10.1016/j.actamat.2020.02.041.

[62] Y. Zhao, J.M. Park, J. il Jang, U. Ramamurty, Bimodality of incipient plastic strength in face-centered cubic high-entropy alloys, Acta Mater. 202 (2021) 124–134. https://doi.org/10.1016/j.actamat.2020.10.066.

[63] Y. Wu, F. Zhang, X. Yuan, H. Huang, X. Wen, Y. Wang, M. Zhang, H. Wu, X. Liu, H. Wang, S. Jiang, Z. Lu, Short-range ordering and its effects on mechanical properties of high-entropy alloys, J. Mater. Sci. Technol. 62 (2021) 214–220. https://doi.org/10.1016/j.jmst.2020.06.018.

[64] R. Zhang, S. Zhao, J. Ding, Y. Chong, T. Jia, C. Ophus, M. Asta, R.O. Ritchie, A.M. Minor, Short-range order and its impact on the CrCoNi medium-entropy alloy, Nature. 581 (2020) 283–287. https://doi.org/10.1038/s41586-020-2275-z.

[65] S.J. Davies, S.P. Jeffs, M.P. Coleman, R.J. Lancaster, Effects of heat treatment on microstructure and creep properties of a laser powder bed fused nickel superalloy, Mater. Des. 159 (2018) 39–46. https://doi.org/10.1016/j.matdes.2018.08.039.

[66] Y.Y. Kaplanskii, P.A. Loginov, A. V. Korotitskiy, M.Y. Bychkova, E.A. Levashov, Influence of heat treatment on the structure evolution and creep deformation behavior of a precipitation hardened B2-(Ni, Fe)Al alloy, Mater. Sci. Eng. A. 786 (2020) 139451. https://doi.org/10.1016/j.msea.2020.139451.

[67] Y.K. Kim, S.H. Park, J.H. Yu, B. AlMangour, K.A. Lee, Improvement in the high-temperature creep properties via heat treatment of Ti-6Al-4V alloy manufactured by selective laser melting, Mater. Sci. Eng. A. 715 (2018) 33–40. https://doi.org/10.1016/j.msea.2017.12.085.

[68] R. Gu, A.H.W. Ngan, Size-dependent creep of duralumin micro-pillars at room temperature, Int. J. Plast. 55 (2014) 219–231. https://doi.org/10.1016/j.ijplas.2013.11.003.

Highlights

- The microstructure and crystallographic orientation-dependent nanomechanical performance of an AM-ed HEA are explored.
- The grain {101} has the highest hardness and elastic modulus, whereas the creep resistance of grain {111} is the greatest.
- The dominate creep mechanism of the AM-ed HEA is lattice diffusion.
- Heat treatment of AM-ed HEA in the current case can increase the hardness and elastic modulus, but decrease the creep resistance slightly.

Supplementary information for

Microstructure and nanomechanical behavior of an additively manufactured $(CrCoNiFe)_{94}Ti_2Al_4$ high-entropy alloy

Siqi Liu [a], Di Wan [b,*], Shuai Guan [c], Yuequn Fu [a], Xiaobo Ren [d], Zhiliang Zhang [a], Jianying He [a,*]

[a] NTNU Nanomechanical Lab, Department of Structural Engineering, Norwegian University of Science and Technology (NTNU), Trondheim 7491, Norway

[b] Department of Mechanical and Industrial Engineering, Norwegian University of Science and Technology (NTNU), Trondheim 7491, Norway

[c] Advanced Manufacturing Technology Research Center, Department of Industrial and Systems Engineering, The Hong Kong Polytechnic University, Hung Hom, Kowloon, Hong Kong

[d] Materials and Nanotechnology, SINTEF Industry, NO- 7465 Trondheim, Norway

[*]Corresponding author.

E-mail addresses: di.wan@ntnu.no (D. Wan), and jianying.he@ntnu.no (J. He).

1. The grains in the three orientations were chosen precisely by the following steps.

1) Firstly, three micro-indents were made on the sample as reference points for the location in both EBSD and nanoindentation.

2) EBSD scans covering the microindents were performed to determine the desired grain orientation (Fig.S1a). The initial point for nanoindentation was determined and its distance to the center of the microindent was accurately measured using SEM (Fig.S1b). Those indents close to the grain boundary were not included in the analysis.

3) Based on the distance measurements, the same location was identified by the optical microscope attached in the nanoindentation testing platform (Fig.S1c). Moreover, the grain boundary morphology of the sample could easily be recognized by the optical microscope, which assisted us to choose the desired crystal orientation to perform the nanoindentation.

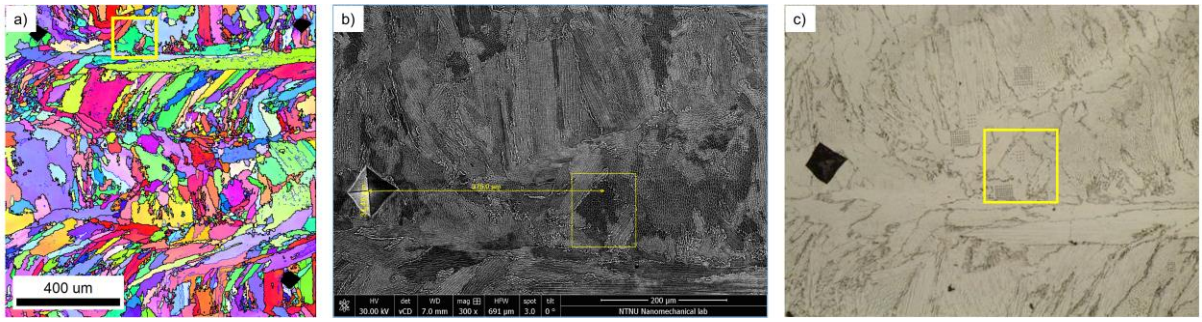

Fig.S1: a) ND-IPF map of the tested area; b) the distance measurements for nanoindentation test; c) optical microscope image under nanoindentation testing platform. The yellow rectangle indicates the tested grain.

2. Grain size distribution from the EBSD data

From the bar chart in Figure S2a, the smaller grains have the higher count in both the as-printed specimen and the heat-treated specimen, where the heat-treated specimen shows a slightly higher count in the smaller grain size range. If we plot the data in a box and whisker chart as Figure R2b, the distribution can be more clearly described. The parameters describing the distribution of the obtained results and are described by the median, mean, first quartile (Q1; the 25th percentile), third quartile (Q3; the 75th percentile), the interquartile range (IQR which is the difference between Q3 and Q1), and outliers (data that lies 1.5 x IQR below or above Q1 or Q3, receptivity) as shown in the illustration in Figure R2c (from ref. [1]). It can be seen that the box and whisker distribution for the as-printed and the heat-treated specimens are rather

similar, showing a slightly higher value in grain size (in diameter) of the as-printed specimen in the median, mean and the interquartile range (25% to 75%).

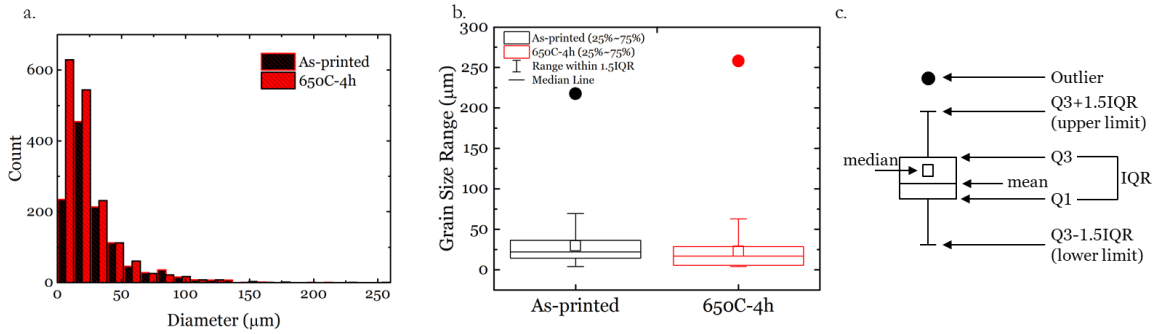

Figure S2: a) bar chart of grain size distribution; b) box and whisker chart of grain size distribution; c) illustration of the box and whisker.

Reference:

[1] A. A. Freeman, D. Wan, C. Bertolin, Examining the effect of indentation separation on the properties of proteinaceous adhesive films made bone gelatine, Proc. Struct. Integr. (2021), (in progress).

3. EDS results showing the (Al,Ti)-rich particle

The chemical composition of the particles has been qualitatively checked by energy-dispersive X-ray spectroscopy (EDS) shown in Figure R3, which shows (Al,Ti)-rich and (Co,Cr,Ni,Fe)-lean composition. The EDS measurement was conducted in an Ultra55 scanning electron microscope (Zeiss) using a Bruker EDS system. The SEM was operated with 10 kV acceleration voltage, 60 μm aperture and ~10 mm working distance.

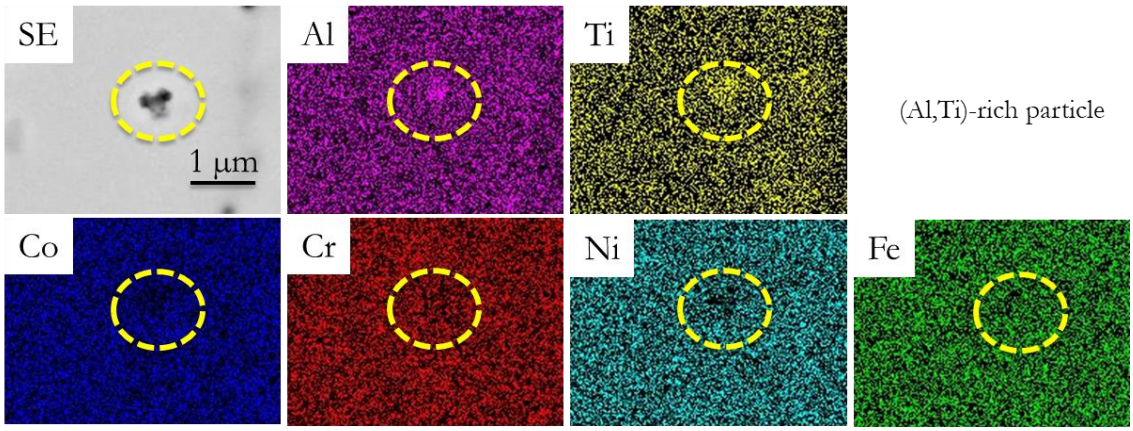

Figure S3: EDS results showing the (Al,Ti)-rich particle.